Materials Today Bio 24 (2024) 100896

Contents lists available at ScienceDirect

Materials Today Bio

journal homepage: www.journals.elsevier.com/materials-today-bio

Functionalized biomimetic mineralized collagen promotes osseointegration of 3D-printed titanium alloy microporous interface

Xiao Sheng [a,1], He Liu [a,b,1], Yu Xu [c], Zhonghan Wang [a,b], Weimin Zhang [a], Chen Li [a,b,*], Jincheng Wang [a,b]

[a] Department of Orthopedics, The Second Hospital of Jilin University, Changchun, 130041, Jilin, China
[b] Orthopaedic Research Institute of Jilin Province, Changchun, 130041, China
[c] Department of Ophthalmologic, The Second Hospital of Jilin University, Changchun, 130041, Jilin, China

ARTICLE INFO

Keywords:
3D-printed porous titanium scaffold
Mineralized collagen
Growth factor
Bionic interface
Angiogenesis
Osseointegration

ABSTRACT

Mineralized collagen (MC) is the fundamental unit of natural bone tissue and can induce bone regeneration. Unmodified MC has poor mechanical properties and a single component, making it unable to cope with complex physiological environment. In this study, we introduced sodium alginate (SA) and vascular endothelial growth factor (VEGF) into the MC material to construct functionalized mineralized collagen (FMC) with good mechanical strength and the ability to continuously release growth factors. The FMC is filled into the pores of 3D printed titanium alloy scaffold to form a new organic-inorganic bioactive interface. With the continuous degradation of FMC, bone marrow mesenchymal stem cells (BMSCs) and vascular endothelial cells (VECs) in the surrounding environment are recruited to the surface of the scaffold to promote bone and vascular regeneration. After implanting the scaffold into the distal femoral defect of rabbits, Micro CT, histological, push-out, as well as immunohistochemical analysis showed that the composite interface can significantly promote osseointegration. These findings provide a new strategy for the development and application of mineralized collagen materials.

1. Introduction

As one of the most profound breakthroughs in orthopedic surgery in the 21st century, joint replacement surgery is an optimal treatment option for various orthopedic conditions [1,2]. In recent years, the use of orthopedic implants for joint replacement has shown an increasing trend, which is expected to continue in the next 15 years [3]. Despite its success in the treatment of necrosis of the femoral head and osteoarthritis diseases, about 10% of patients suffered surgical failure and need revision surgery [4,5]. In addition to microbial infections, poor osseointegration between bone and implant is an important cause of surgical failure [6,7].

Osseointegration is defined as a strong bond between the implant and surrounding bone tissue, playing a major role in maintaining the long-term stability of the implant [8]. When the prosthesis is implanted into the patient's body, BMSCs are continuously recruited to the surface of the implant. In the following days to months, BMSCs continuously differentiate into osteoblast precursors and secrete extracellular matrix (ECM) to reshape the microenvironment of the prosthesis interface [9]. At the same time, new bone formed around the implant will be mineralized and eventually lead to bone integration [10,11]. In this complex process, the characteristic of implant material is one of the key factors affecting the microenvironment of osteogenesis.

With advances in manufacturing technology, cell biology, molecular biology and material science, orthopedic implants have witnessed rapid progress [12–15]. Compared with the first generation of implants that can only provide mechanical support, the new generation orthopedic implant is designed to provide improved bone conductivity, induction and integration [16]. Titanium alloy has become a popular material of choice for orthopedic implants due to its good biocompatibility, low elastic modulus and plasticity [17]. With the advent of three-dimensional (3D) printed technology, researchers can design titanium alloy implants that match the shape of bone tissue based on the individual imaging data [18]. Moreover, 3D printed technology can simulate the porous structure of natural bone and adjust the elastic modulus of titanium alloy implants, greatly reducing the risk of

* Corresponding author. Department of Orthopedics, The Second Hospital of Jilin University, Changchun, 130041, Jilin, China.
E-mail addresses: 943889051@qq.com (X. Sheng), heliu@jlu.edu.cn (H. Liu), 1013263162@qq.com (Y. Xu), zhonghan19@mails.jlu.edu.cn (Z. Wang), z1933554836@qq.com (W. Zhang), chenliortho@jlu.edu.cn (C. Li), jinchengwangjlu@163.com (J. Wang).
[1] These authors have contributed equally to this work and share first authorship.

https://doi.org/10.1016/j.mtbio.2023.100896
Received 11 May 2023; Received in revised form 11 October 2023; Accepted 30 November 2023
Available online 5 December 2023

osteolysis around the prosthesis and facilitating surgery [19,20].

Although the mechanical property provided by titanium alloy prostheses is sufficient to meet the mechanical support of the load-bearing area, the biological inertness and smooth surface of titanium alloy materials make it difficult for osteoblasts to adhere [17]. This may be one of the reasons why titanium alloy implants are prone to poor osseointegration. To solve this difficult problem, many studies have attempted to change the surface morphology and chemical composition of titanium alloys surface [21]. Although these methods have shown certain positive effects, their effectiveness in improving osteogenic activity is limited. In recent years, the study of biomimetic prosthetic interfaces has received widespread attention in the field of biomaterials. Some researchers are committed to creating a prosthetic interface with components and structures similar to natural bone tissue to promote osseointegration.

Mineralized collagen (MC) is the basic unit of natural bone tissue, which is mainly composed of collagen type 1 (Col-1) (20%–30%) and hydroxyapatite (60%–70%) [22]. Col-1 has the nucleation site of apatite crystal particles, which can guide the growth and arrangement of mineral crystals [23,24]. Inspired by bionics, researchers have synthesized bone substitutes that mimic natural MC and achieved amazing results. These biomimetic materials exhibited excellent biocompatibility and biodegradability both *in vivo* and *in vitro*, and effectively promote bone defect repair or bone integration [25]. In situ deposition is one of the main methods to prepare mineralized collagen, that is, Ca^{2+} and PO_4^{3-} are introduced into the collagen solution and adjusted the PH to neutral to trigger the self-assembly and mineralization of collagen fibers [26]. Although this method is simple, the mechanical properties of the mineralized collagen obtained are extremely poor, making it unable to exert its biological effects as a scaffold and coating [27]. Therefore, researchers often add certain polymers to mineralized collagen to endow it with stronger physicochemical properties and biological functions [28].

Alginate is a natural polymer that is a byproduct of extracting iodine and mannitol from kelp or sargassum [29]. Under mild conditions, sodium alginate (SA) can cross link with Ca^{2+} to form a firm gel structure [30]. Some studies have shown that adding alginate to the collagen system will form thicker fibrils and mechanically enhanced hydrogels with Ca^{2+} capture capacity [31]. Furthermore, SA also gives MC materials more flexibility. This is because SA can be used as a carrier for a variety of therapeutic elements (cells, antibiotics and growth factors) [32]. Compared with pure MC, SA/MC composite materials can better sustainably release drugs and maintain biological activity for a long time [33]. VEGF, as a potent angiogenic factor, can induce vascular regeneration by recruiting endothelial cells and upregulating various genes such as MMP-2, HIF-1, and KDR [34]. Functional mineralized collagen (FMC) was obtained by injecting VEGF-loaded sodium alginate into MC materials. FMC can slowly release signaling factors in a humid environment in the body, forming a concentration gradient around the implant, stimulating bone marrow mesenchymal stem cells (BMSCs) osteogenic differentiation and migrating vascular endothelial cells (VECs) towards to the center of the implant, completing cell recruitment, and promoting vascular regeneration to provide oxygen and nutrition, accelerating bone regeneration at the implant interface [33,35].

In this study, we developed a FMC to construct a cell microenvironment conducive to osteogenesis, and systematically detected the BMSCs and VECs behavior including viability, proliferation and differentiation. The FMC was combined with 3D printed titanium alloy porous scaffold to construct a new bioactive prosthesis interface (sTi/VEGF) and implant into the bone defect of the distal femur of rabbits. *In vitro*, sTi/VEGF not only promotes the proliferation and osteogenic differentiation of BMSCs, induces VECs aggregation, but also increases the expression of osteogenic and vascular related genes. *In vivo*, collagen, calcium phosphate, and VEGF released by sTi/VEGF enhances the regeneration of bone and blood vessels on the surface of the prosthesis, thus promoting osseointegration at the prosthesis interface. (Scheme 1).

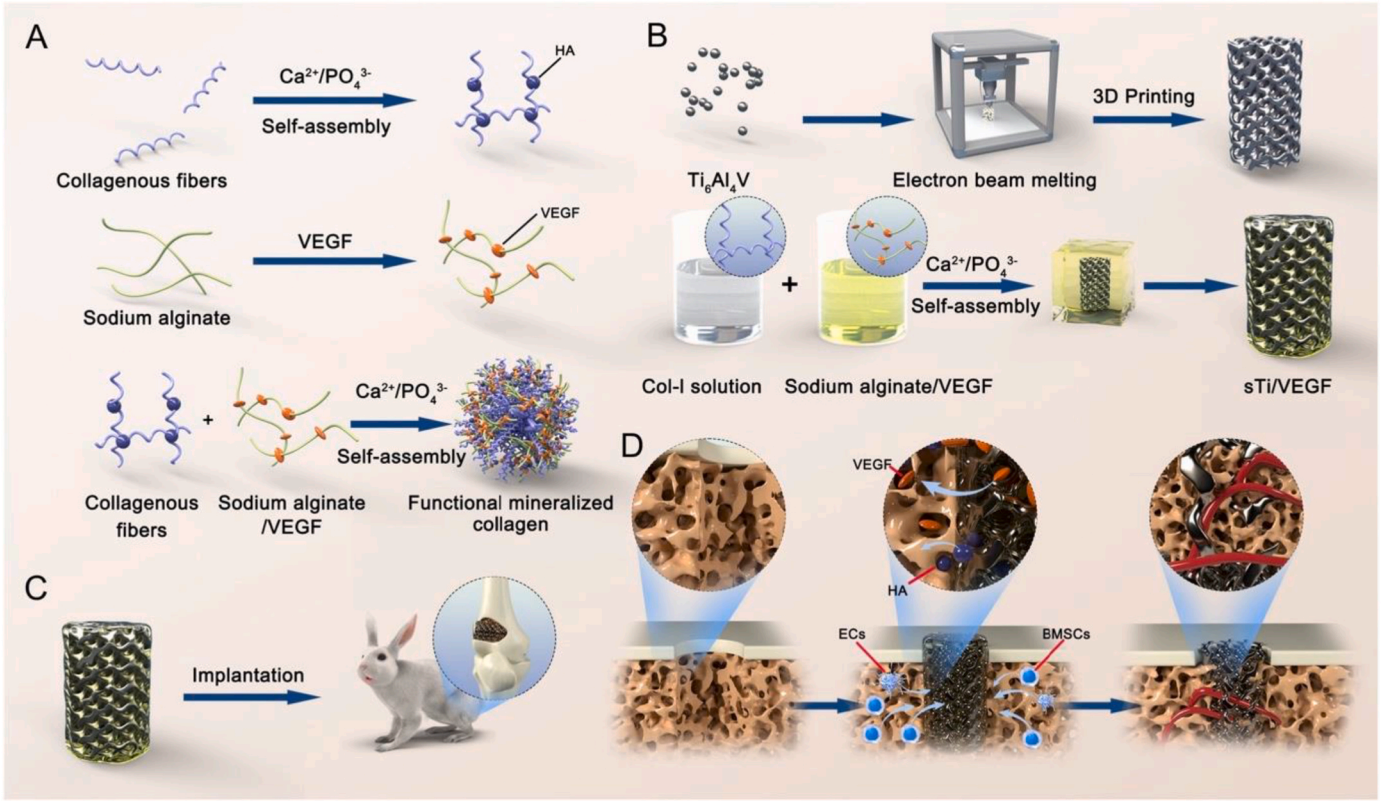

Scheme 1. Schematic illustration. (A) Synthesis of Functional mineralized collagen. (B) Preparation of sTi/VEGF. (C) Implantation of sTi/VEGF into distal femoral bone defects in rabbits. (D). High-quality osseointegration achieved after implantation of bioactive prosthesis interfaces.

2. Materials and methods

2.1. Preparation of 3D printed porous titanium alloy scaffold

We designed disc-shaped (φ10 mm × L3 mm) and cylindrical (φ4mm × L8 mm) porous titanium alloy scaffolds for *in vitro* and animal experiments, respectively. The two types of scaffolds shared some common parameters, including porosity = 70%, pore size = 765 μm, and strut size = 300 μm. The titanium alloy bracket was manufactured using the electron beam melting (EBM) system (EOS M280, Germany). Briefly, we developed disk-shaped and cylindrical 3D models and converted them into standard triangulation language files, which were exported to the EBM machine. According to the data, medical grade Ti_6Al_4V powder (TLS, Germany; sphere with a diameter of 45–55 μm) was melted layer by layer and cooled to form a solid. All samples were cleaned with ultrasonic wave in acetone, ethanol and deionized water for 15 min. Subsequently, the scaffolds were autoclaved at 121 °C for 20 min and then maintained at 60 °C in an oven. Finally, all samples were exposed to ultraviolet light for 24 h for subsequent experiments.

2.2. Preparation of FMC and construction of functional bionic interface

Briefly, we dissolve 0.15 g of SA (Solar, Beijing, China) powder in 5 ml of deionized water, mix it with magnetic force for 1 h at 50 °C to obtain 3% SA solution. Then, placed the obtained SA into a centrifuge tube and sterilize it in a high-pressure steam sterilization pot, and let it stand for 24 h at 4 °C. Next, we mixed sterile Col-1(Corning, USA) solution with 3% SA 1:1 to form a viscous liquid. We then added VEGF (PeProTech, USA) solution prepared according to the manufacturer's instructions. VEGF was dissolved in sterile PBS containing 5% trehalose and then diluted into a solution that could be used for a long time. It has been shown that VEGF exhibits the best angiogenesis and osteogenesis induction effect at a concentration of 25 ng/ml [36]. Therefore, we added VEGF into the above solution to obtain a final concentration of 25 ng/ml and 2.5 μg/ml *in vitro* and *in vivo*, respectively. Finally, we sequentially added 0.1 M Na_2HPO_4 and 0.1 M $CaCl_2$ solutions to the above mixed solution and adjusted the pH to 7.35–7.45 using 0.1 M NaOH to trigger mineralization.3D printed Ti_6Al_4V scaffolds were placed into this hydrogel, which allowed the hydrogel to infiltrate their internal microporous structure under the vacuum pump to obtain the composite interfaces (sTi/VEGF) required for this experiment.

2.3. Material characterization of sTi/VEGF

The microstructure of sTi/VEGF was observed using scanning electron microscopy (SEM; SU-8100, Hitachi, JPN). The elemental and phase composition were quantified by energy-dispersive X-ray spectroscopy (EDS; IXRF3310, USA) and X-ray diffraction (XRD; Bruker, GER), respectively. Fourier-transform infrared spectroscopy (FTIR; TFN 6700, USA) was used to analyze functional groups in materials within the wave number range of 550–4000 cm^{-1}.

2.4. VEGF release in vitro

In order to test the release rate of growth factors in sTi/VEGF, we placed the prepared sTi/VEGF in 24 well plates (Corning, USA) and added 1 ml PBS (Solar Beijing, China). All samples were incubated in a cell incubator at 37 °C. Then, PBS solution containing VEGF were collected for ELISA detection at predetermined time points (0, 1, 4, 7, 14, 21, and 28 days). Enzyme-linked immunosorbent assay (ELISA; R&D Systems, USA) was used to detect the concentration of VEGF in PBS and plot a standard curve to calculate the cumulative release amount of VEGF.

2.5. Degradation rate of FMC in vivo

To evaluate the degradation rate of the FMC *in vivo*, we implanted 1 ml hydrogel under skin. The rats were killed by spinal dislocation at the predetermined time points (1, 4, 7, 14, 21 and 28 days). Then, we removed the FMC from the tissue and weighed. The degradation rate of the FMC at each time point was calculated according to the weight of the FMC injected subcutaneously into the rat at the beginning, and the degradation curve of the hydrogel was drawn.

2.6. Rheological properties of hydrogel

The US302 rheometer was used for the rheological test of the hydrogel. Before the test, the hydrogel prepolymer was prepared by the mold and placed in the quartz mold (diameter: 15 mm, height: 2 mm). After 10 s of illumination, the obtained gel sample was placed in the rheometer clamp. The outer layer of the hydrogel was sealed with silicone oil to reduce errors caused by water evaporation of the hydrogel. Gel samples were prepared at constant frequency (1 Hz) and constant strain (0.5%).

2.7. In vitro cell experiments

2.7.1. Culture of BMSCs and HUVECs

BMSCs were isolated from the bone marrow of femur and tibia of suckling rabbits (1 week old). Briefly, the rabbits were killed by injecting air into the ear vein and put into a beaker containing 75% alcohol. Next, we transfer the suckling rabbits to a cell culture dish and their femur and tibia were dissected. After removing the peripheral soft tissue, the bone was removed from the metaphysis, and the BMSCs in bone marrow was washed in F-12 medium (Gibco, NY, USA) containing 10% fetal bovine serum and 1% penicillin/streptomycin (Hyclone, USA). Then, the BMSCs were incubated in cell incubator at 37 °C and 5% CO_2 and the cells were passaged when they completely covered the bottom of the culture dish. After cells passage to the third generation, BMSCs were used for cytotoxicity testing and osteogenic differentiation assay.

The HUVECs were purchased from Cellcook Biotech (Guangzhou, China). Cells were incubated in high-sugar medium (Gibco, NY, USA) containing 10% fetal bovine serum and 1% penicillin/streptomycin at 37 °C and 5% CO_2, with the medium changed every two days. The cells were passaged after they completely covered the bottom of the cell culture dish. In this study, cells from the 3rd to the 6th generation were used.

2.7.2. Cell phenotype identification by flow cytometry

Flow cytometry was used to identify surface antigens of BMSCs and HUVECs. Briefly, BMSCs were placed in a centrifuge tube and treated with 50% ethanol for 30 min. A single cell suspension of 100 μl was prepared by centrifugation, and primary antibodies (CD34, CD90) were added. The supernatant was removed by centrifugation after incubating at room temperature for 30 min. FITC labeled secondary antibodies were added and incubated in dark for 30 min at 4 °C. PBS was washed and centrifuged to remove the supernatant, and resuspended cells by re adding PBS. The samples in the flow cytometry tube were tested. The same method was used to detect HUVECs surface antigens (CD31, CD34).

2.7.3. Cell viability

The live-dead cell staining (BestBio, Shanghai, China) and CCK-8 assay (Bioss, Beijing, China) were used to evaluate the cell viability of sTi/VEGF. For live-dead cell staining, empty titanium (eTi), SA/MC bound titanium (sTi) and sTi/VEGF were placed into 24-well plates. Subsequently, 2 ml medium suspension (2×10^4/well) BMSCs were added to each group. BMSCs were cultured for 24 h. Next, scaffolds in each group were then immersed in the live/dead cell staining solution and incubated at 37 °C under dark conditions for 15 min. After removing

the working solution and washing with PBS, the stained BMSCs were observed under a fluorescence microscope (Olympus, JAN).

For the CCK-8 assay, eTi, sTi, and sTi/VEGF were placed in 24-well plates, and 2 ml of BMSCs suspension (2×10^4/well) was added into each group. BMSCs were then cultured for 1, 4, and 7 days. Next, each group was then immersed in the CCK-8 solution and incubated at 37 °C for 2 h. The absorbance was measured at 450 nm using a Microplate Reader (BioTek Instruments, USA).

2.7.4. Angiogenic activity of sTi/VEGF

2.7.4.1. Cell invasion assay. HUVECs were starved and incubated for 12 h before the experiment. The cells were then resuspended in a serum free medium and 100 μl (2×10^4/well) was added to the upper chamber of a 24-well Transwell insert (Corning, USA). Then, scaffolds in each group was placed in the lower chamber with 300 μL complete medium containing FBS. After incubating at 37 °C and 5% CO_2 for 24 h, the HUVECs were fixed in 4% paraformaldehyde (Solar Beijing, China) for 20 min and then washed three times with PBS. Finally, the cells in the lower chamber were stained with crystal violet (0.1% g/ml) for 10 min and observed under microscope and quantitatively analyzed using Image J software.

2.7.4.2. Wound healing assay. HUVECs were seeded in 6-well plates at a concentration of 1×10^6/well and cultured for 12 h. When cells reach 80% fusion, a single scratch was made with 200 μL pipette tip on the bottom of the culture plate. Each well was washed three times with PBS to remove any cell debris. Subsequently, scaffolds in each group was placed in 6-well plate and co-cultured with HUVECs. After 24 h, the repair of scratch was observed under a microscope and quantitatively analyzed using Image J software.

2.7.4.3. Tube formation assay. The Matrigel matrix (BD, United States), 96-well plate, and gun head were maintained at 4 °C for 12 h before the experiment. Then, 50 μL Matrigel matrix was poured into a 96 well plate and maintained at 37 °C for 30 min. Then, HUVECs were resuspended in extracts from eTi, sTi and sTi/VEGF and inoculated on the surface of matrix at a concentration of 1×10^4 cells/well. After 6 h of incubation, tubes were observed under an inverted microscope. The results were analyzed quantitatively with Image J software.

2.7.4.4. Real-time quantitative polymerase chain reaction (RT-qPCR) for angiogenesis genes. To evaluate the effect of the sTi/VEGF on angiogenesis genes (*MMP-2*, *Bax* and *Bcl-2*), HUVECs were cultured in 6-well plates (1×10^6/well) for 1 and 4 days with eTi, sTi and sTi/VEGF. Total cellular RNA was extracted with RNA extraction kit (Beyotime, Shanghai, China) and reversed transcribed to cDNA using cDNA synthesis kit (Beyotime, Shanghai, China) following the manufacturer's instructions. The expression levels of mRNA were detected using Q SYBR green Supermix (Bio-Rad, Hercules CA, USA) and QuantStudioTM 7 Flex real-time PCR system (Applied Biosystems, Carlsbad, CA, USA). Finally, the relative gene expression levels were calculated using the comparative Ct method ($2^{-\triangle\triangle Ct}$) and normalized based on the expression levels of the endogenous human *GAPDH* gene.

2.7.5. Osteogenic differentiation of sTi/VEGF

2.7.5.1. ALP staining and quantitative analysis. For ALP staining, BMSCs (2×10^4/well) were inoculated on eTi, sTi, sTi/VEGF in 24-wells plates and cultured with osteogenic differentiation medium (OriCell, Guangzhou, China). After 7 and 14 days of incubation, each group was stained using the ALP staining kit (Beyotime, Shanghai, China). In brief, the medium was aspirated from the 24-wells plates that were then washed with PBS. The cells were fixed with 4% paraformaldehyde for 30 min and washed with PBS again. Subsequently, ALP staining solution was added into the 24-wells and incubated for 2 h. Finally, the staining cells were observed under an optical microscope.

For ALP quantitative analysis, BMSCs (2×10^4/well) were inoculated on eTi, sTi, sTi/VEGF in 24-wells plates and cultured with osteogenic differentiation medium. After 7 and 14 days of incubation, each group of cells was lysed using cell lysate (Beyotime, Shanghai, China). The ALP activity of cells was detected using the ALP assay kit (Beyotime, Shanghai, China).

2.7.5.2. RT-qPCR for osteogenesis genes. To evaluate the expression of osteogenic genes (*BMP-2, ALP* and *OCN*) in the cells, BMSCs were inoculated on eTi, sTi and sTi/VEGF in 6-wells plates and cultured with differentiation medium. After 7 and 14 days, total cellular RNA was extracted by RNA extraction kit and reversed transcribed to cDNA by cDNA synthesis kit following the manufacturer's instructions. The expression level of mRNA was detected using Q SYBR green Supermix and QuantStudioTM 7 Flex real-time PCR system. Finally, the relative gene expression levels were calculated using the comparative the Ct method ($2^{-\triangle\triangle Ct}$) and normalized based on the expression of the endogenous human *GAPDH* gene.

2.8. Animal experiments

Animal experiments were performed in compliance with the National Institutes of Health's Guide for the Care and Use of Laboratory Animals (NIH Publications No. 8023, revised 1978) and were approved by the Animal Care and Use Ethics Committee of Jilin University. 60 New Zealand white rabbits (6 months, 3 ± 0.5 kg) were randomly divided into three groups: eTi, sTi and sTi/VEGF. Rabbits were anesthetized with 3% pentobarbital at a dose of 60 mg/kg. According to the size of the scaffolds, a cylindrical bone defect with a radius of 4 mm radius and a height of 12 mm was created on the lateral epicondyle of the femur using an electric drill. After washing with normal saline, scaffold was placed into the defect and sutured with absorbable suture. Penicillin (2 mg/kg) was injected intramuscularly 3 days after operation. At the 12th week after operation, rabbits were euthanized using auricular vein air injection, and their distal femurs were removed and fixed in 4% paraformaldehyde.

2.8.1. Microscopic computed tomography (micro CT) analysis

Micro CT was used to evaluate the growth of bone into the porous of scaffold. Samples were scanned at 48 kV voltage, 200 μA current and 18 μm Imagepixel size using Skyscan 1076 scanner (Bruker Micro CT, NV, Konich, Belgium) to obtain 3D visual reconstruction of scanned images. Then, image analysis was performed using a bone analyzer (CT analyzer 1.17.7.2 software, Konich, Belgium). In Micro CT analysis, the size of the region of interest was the area where the stent was located. Finally, various parameters, including bone volume fraction (BV/TV), trabecular number (Tb. N), trabecular arthritis (Tb. Th) and trabecular separation (Tb. SP) were measured from the collected images.

2.8.2. Push-out mechanical test

To evaluate the bonding strength between the interface and bone, we conducted a mechanical push out experiment. In brief, the soft tissues around each bone were removed to reveal the interface position. Then, a hydraulic testing machine (MTS Mini Bionix, Minneapolis, USA) was used to press the position of the interface at a speed of 1 mm/min to separate the interface from the bone. Finally, the maximum thrust needed to detach the implant from the bone tissue was recorded and analyzed.

2.8.3. Histological evaluation

Samples were fixed with 4% paraformaldehyde solution for 2 weeks and then decalcified for 4 weeks. Subsequently, samples were dehydrated using an ethanol gradient. After vitrification with xylene, the

samples were embedded in paraffin, cut into thick sections, stained with VG and Masson and were observed under a microscope (DSX 500; Olympus Corporation, Tokyo, Japan). The surface area and growth depth of new bone was analyzed using Image J.

2.8.4. Immunohistochemistry

Rabbit femur samples were fixed in 4% paraformaldehyde for 2 weeks, and scaffold was removed after decalcification. The remaining bone tissue was sectioned and stained. In brief, the sections of the treated femoral specimens were treated with 3% H_2O_2, blocked in serum and incubated with specific antibodies against the angiogenic markers CD31 and CD34 and osteogenic markers OCN and Col-1 overnight at 4 °C. After further incubation with a secondary antibody, these antibody-labeled sections were stained with diaminobenzidine and hematoxylin, dehydrated in an alcohol gradient, and sealed. Finally, the sections were observed under a microscope.

2.9. Statistical analysis

Data are presented as mean ± standard deviation. Each group of data was obtained from three independent experiments. Differences between multiple experimental groups were statistically analyzed using one-way analysis of variance (ANOVA) and Tukey's multiple comparison test. Prism 9 was utilized for all statistical analysis. $P < 0.05$ indicated significant difference.

3. Results

3.1. Characterization of the sTi/VEGF

The appearance of MC and FMC is shown in Fig. S1. We can clearly observe that The addition of SA changes the viscous MC liquid into gel state. As shown in Fig. S2A, the disc-shaped scaffold and cylindrical scaffold measured 3 mm and 8 mm in height and 10 mm and 4 mm in diameter respectively and hydrogel completely fills the pores of the scaffold (Fig. S2B), which is more conducive to cell proliferation and adhesion. Empty scaffolds had a pore diameter of 765 (Fig. S3)μm and porosity of 70%, with the titanium alloy scaffold surface having micron level roughness (Fig. 1A(a)). EDS analysis showed that the presence of C, N, O, Ca and P (Fig. S4) which confirmed the combination of FMC and titanium alloy scaffold is successful.

To further determine the crystal structure in materials, the MC and FMC were analyzed by XRD after freeze-drying. As shown in Fig. S5, multiple characteristic peaks of HA were observed in both MC and FMC. According to Fig. S5A, peak observed at 2θ degree of 31.7 can be recognized to (211) HA crystal lattice. In FMC (Fig. S5B), peaks observed at 2θ degree of 27.6, 31.8, 32.2, and 45.7 can be recognized to (102), (211), (112), and (222) HA crystal lattice. It can be seen that the addition of SA contributes to the formation of HA with different lattices.

The absorption bands of MC and FMC were obtained through FTIR. The characteristic banding of the PO_4^{3-} group can be seen in both samples (Fig. S6), with asymmetric O–P–O bending modes occurring at approximately 574 cm^{-1} and asymmetric P–O stretching modes occurring at approximately 1028 cm^{-1} and 1057 cm^{-1}. As expected, N–H

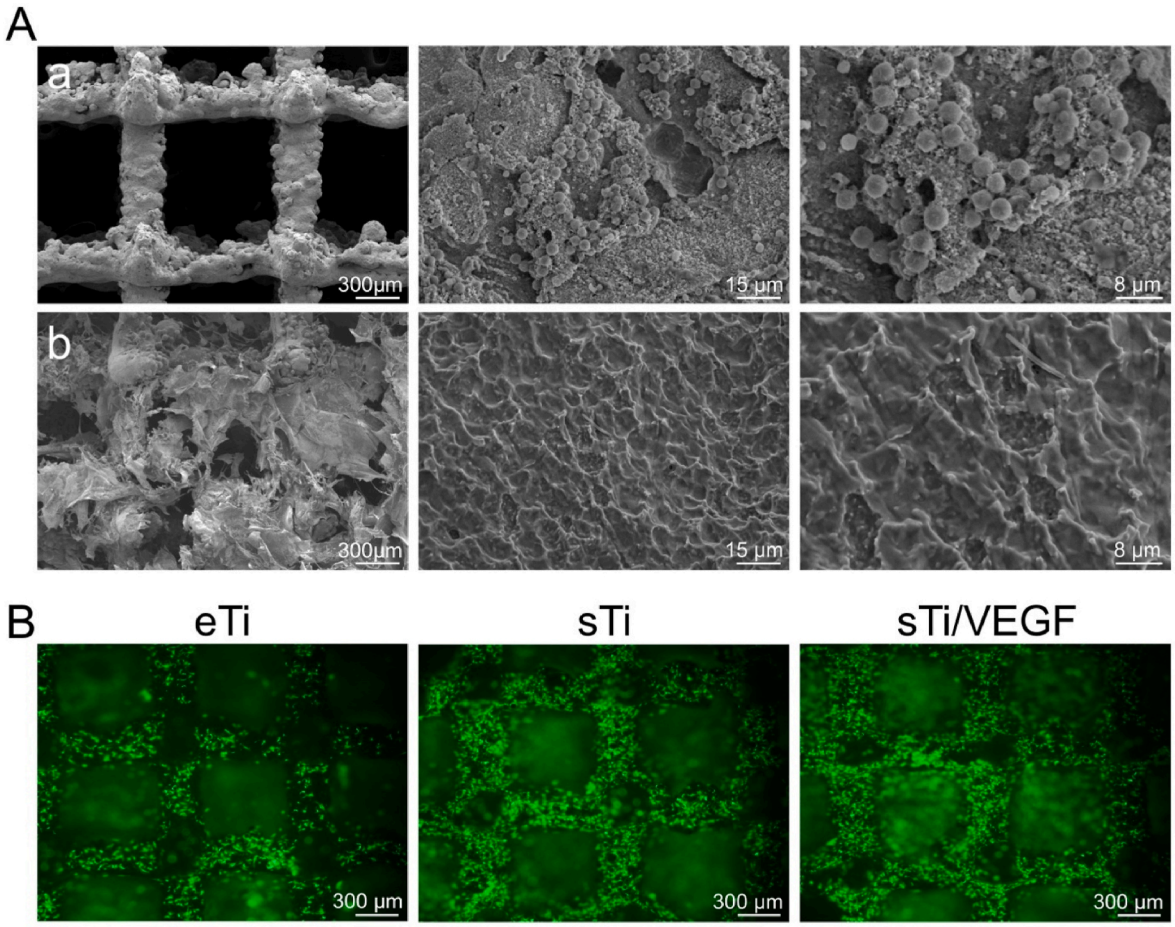

Fig. 1. Microscopic characterization of (A) eTi (a) and (b) sTi/VEGF using SEM scanning images. (B) Live (green)/dead (red) staining of BMSCs cultured with eTi, sTi, sTi/VEGF for 24 h. (For interpretation of the references to color in this figure legend, the reader is referred to the Web version of this article.)

absorption peaks of collagen amide were observed between 3414 cm^{-1} in MC. Double peaks also appeared near 1641 cm^{-1} and 1548 cm^{-1}, and a peak also appeared at 857 cm^{-1}, which is due to the replacement of apatite vibration frequency by carbonate ions at the phosphate and OH^- positions. The absorption peak near 1641 cm^{-1} on the spectra of MC is most likely attributed to OH^-, CO_3^{2-}, H_2O, or a combination of the contribution of the former and the amide I band of collagen [37]. Stretching vibration of N–H group of collagen and SA was observed near 3294 cm^{-1}. The stretching vibration of aliphatic C–H of collagen and SA was observed at 2887 cm^{-1} and 2827 cm^{-1}, respectively. In addition, we also observed an absorption peak of –COOH at 1605 cm^{-1} [38]. In summary, there is a significant difference in the FTIR spectra of MC and FMC, with varying degrees of shift in the absorption peak positions, which explains the interaction between collagen and SA.

3.2. Ability of sTi/VEGF to release VEGF

We detected the amount of VEGF released by sTi/VEGF at each predetermined time point by ELISA. The cumulative release of VEGF in the sTi/VEGF within 28 days is shown in Fig. S7A. It showed that FMC released 32.48% ± 1.2% VEGF within the first 24 h. Subsequently, the release rate gradually slowed down and stabilized. At 28 days, FMC released a cumulative 79.22% ± 2.17% of VEGF.

3.3. Rheological properties

We used a rheometer to characterize the shear viscosity and shear stress of MC and FMC. Shear stress is the interaction force that occurs between two sides of any cross-section (shear plane) inside an object when it deforms due to external factors such as load and temperature changes (Fig. S9A). The ratio of shear stress to shear rate is called shear viscosity. Shear viscosity is a measure of the viscosity of hydrogel, and it is an expression of fluid flow force on its internal friction phenomenon. The higher shear viscosity means that the hydrogel has a strong ability to maintain its own shape stability. This also proves that high shear viscosity hydrogels have better mechanical properties. As shown in Fig. S9B, when the shear rate is the same, the shear viscosity of FMC is greater than that of MC, indicating that FMC has better mechanical strength.

3.4. Degradation of FMC in rats vivo

We measured the degradation rate of hydrogel *in vivo* by subcutaneous implantation in rats (Fig. S8). As shown in Fig. S7B, FMC degraded by 33.66% ± 5.87% in the first week, and then the degradation gradually slowed down. At 28 days, FMC had a cumulative degradation rate of 70.71 ± 2.93%.

3.5. In vitro cell experiments

3.5.1. Cell phenotype identification by flow cytometry

Detection of surface antigens of BMSCs and HUVECs by flow cytometry. As shown in Fig. S10, BMSCs showed positive expression of CD90 and negative expression of CD34, while HUVECs showed positive expression of CD31 and CD34. This is consistent with the typical cell surface antigen expression characteristics of BMSCs and HUVECs.

3.5.2. Cells viability and proliferation

The live-death staining assay was used to evaluate the biocompatibility of each type of scaffold. As shown in Fig. 1B, after co-culture of eTi, sTi and sTi/VEGF with BMSCs for 24 h, more living cells were recorded on the surface of sTi and sTi/VEGF, and only a few cells were attached on the surface of eTi. This demonstrated that FMC not only has good biocompatibility but also provides more cells attachment points and survival space for the surface of titanium alloy scaffolds.

The CCK-8 assay was conducted to quantified assess the effect of each type of scaffold on cell proliferation. As shown in Fig. S11, the cells in all groups were in a proliferative state at all time-points, indicating the good biocompatibility of the prepared titanium scaffolds. At 4 days, sTi and sTi/VEGF did not show the effect of promoting cell proliferation. Until the 7th day, sTi/VEGF exhibited higher proliferation rates than cells in the sTi ($P > 0.05$). This may be due to the explosive release of growth factors causing a slight cellular inhibitory effect. As the release of growth factors stabilizes, the effect of sTi/VEGF on promoting cell proliferation is gradually demonstrated.

3.5.3. Effect of sTi/VEGF on angiogenesis

3.5.3.1. Cellular migration. The effect of different scaffolds on the migration ability of HUVECs were assessed through the cell invasion assay and wound healing assay. In the invasion experiment, the penetration ratio of sTi/VEGF group cells was 2.44 ± 0.60-fold and 1.53 ± 0.15-fold that in eTi and sTi groups (Fig. 2A). In the wound healing assay, the maximum fluidity was observed in the sTi/VEGF group (Fig. 2B). This indicated that VEGF is a key factor inducing the migration of HUVECs. Therefore, we demonstrated that sTi/VEGF induces targeted migration of HUVECs through sustained release of growth factors.

3.5.3.2. Tubule formation. The tubule formation was performed to assess the angiogenesis activity of the different scaffolds. After 6 h of culture, microscopic observation revealed that the HUVECs formed a tubular structure (Fig. 2C), and the total length was analyzed with image J (Fig. 2F). The results showed that the total length of tubules in sTi/VEGF group was 1.34 ± 0.18-fold and 1.28 ± 0.12-fold higher compared with that of eTi and sTi groups, respectively. Tubular formation simulates the basic process of angiogenesis, which suggests that sTi/VEGF can induce the formation of tubular structures in HUVECs at the implantation site, providing conditions for final angiogenesis.

3.5.3.3. RT-PCR of angiogenesis genes. To further evaluate the angiogenesis activity of different scaffold *in vitro*, the expression of three genes related to angiogenesis was measured. MMP-2 is a marker of angiogenesis and remodeling [39]. As shown in Fig. 3F, the mRNA level of MMP-2 in sTi/VEGF was 2.05 ± 0.0.78-fold and 3.49 ± 0.26-fold higher than that in eTi on days 1 and 4. Bax is the most important apoptosis gene in human cells [40]. The mRNA level of Bax was higher by 0.21 ± 0.05-fold and 0.25 ± 0.03-fold in sTi/VEGF cultured HUVECs compared to eTi on days 1 and 4 (Fig. 3H). Bcl-2, in contrast to Bax, can inhibit cell apoptosis [41]. On days 1 and 4, the mRNA level of Bcl-2 in sTi/VEGF was 3.12 ± 0.39-fold and 3.15 ± 0.41-fold higher compared with that of eTi respectively (Fig. 3G). These results demonstrate that sTi/VEGF stimulates the expression of genes related to angiogenesis. In addition, the expression level of anti-endothelial cell apoptosis gene in sTi/VEGF increases and the expression level of promoting apoptosis decreases.

3.5.4. Effect of sTi/VEGF on osteogenesis

3.5.4.1. ALP staining and quantitative analysis. The content of ALP in BMSCs can reflect the osteogenic potential. To evaluate the osteogenic induction ability of different scaffolds on BMSCs, we conducted ALP staining and ALP quantitative analysis. As shown in Fig. 3A, we found that the staining depth of cells at 14 days was significantly higher than at 7 days in the same group. Comparison between groups showed that the staining intensity in sTi and sTi/VEGF groups was significantly deeper than in eTi group. In addition, the sTi/VEGF group had the highest ALP staining intensity. These findings were verified in the ALP quantitative assay (Fig. 3B). This confirmed that mineralized collagen can promote the osteogenic differentiation of stem cells. In addition, VEGF and mineralized collagen may have synergistic effects in stimulating the osteoblastic differentiation and proliferation of cells.

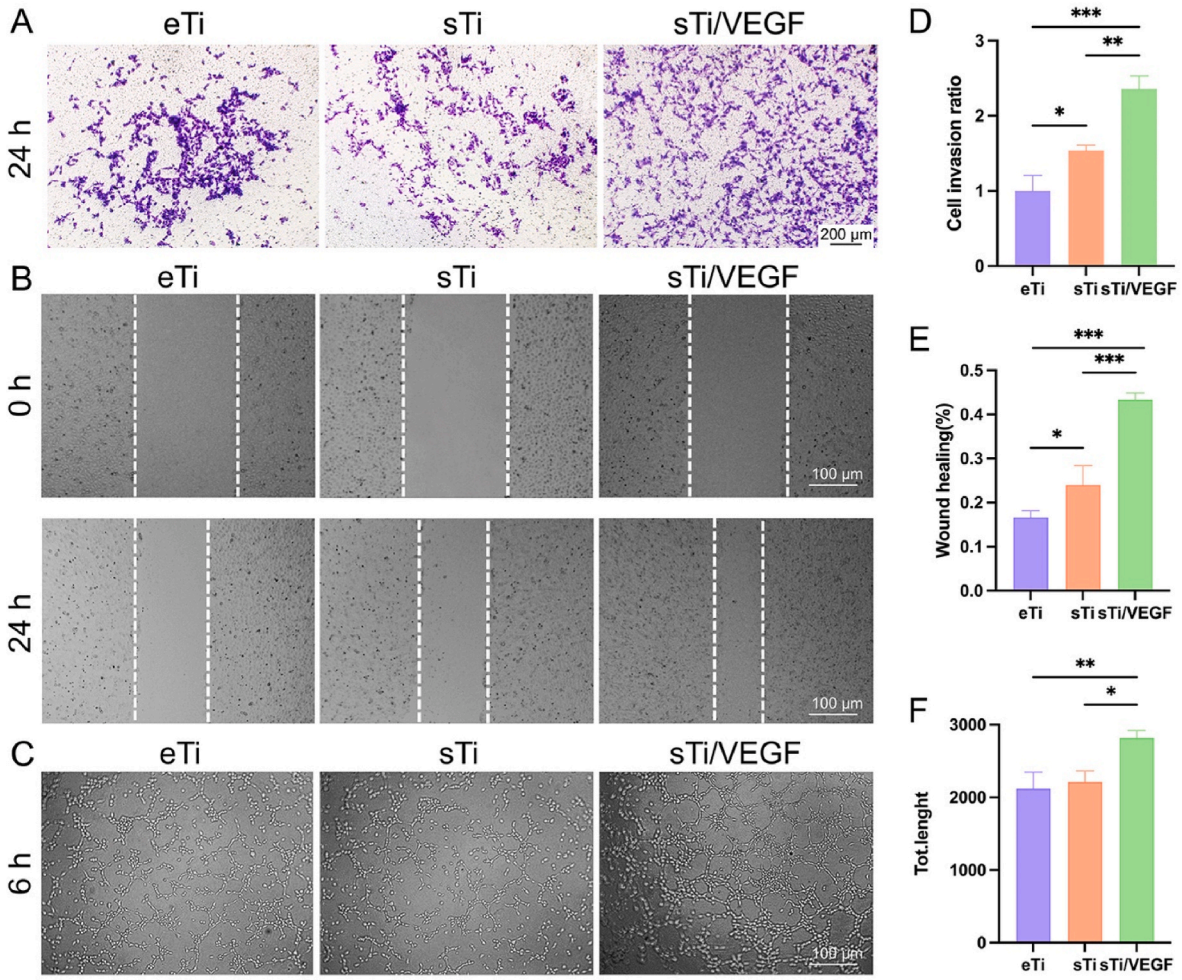

Fig. 2. Effects of different scaffolds on cellular migration and angiogenesis (A) Effects of eTi, sTi and sTi/VEGF on HUVECs invasion. (B) Effects of eTi, sTi and sTi/VEGF on wound healing as examined under microscope. (C) Tube formation by HUVECs cultured with eTi, sTi and sTi/VEGF extracts for 6 h. (D) Quantitative analysis of HUVECs stained with crystal violet. (E) Assessment of wound healing rates. (F) Total length of tube after treatment with different interfaces (n = 3, *indicates significant differences between the groups; *p < 0.05; **p < 0.01; ***p < 0.001). (For interpretation of the references to color in this figure legend, the reader is referred to the Web version of this article.)

3.5.4.2. RT-PCR of osteogenesis genes. Three osteogenesis-related genes including ALP, BMP-2 and OCN were detected through the RT-PCR experiment. ALP is a significant early osteogenic marker of stem cells differentiation into the osteogenic phenotype [42]. As shown in Fig. 3C, the mRNA levels of ALP were higher by 2.19 ± 0.45-fold and 1.91 ± 0.44-fold in sTi/VEGF cultured BMSCs compared with levels in eTi and sTi groups on day 7, and were higher by 2.19 ± 0.47-fold and 1.16 ± 0.57-fold on day 14. BMP-2 is a member of the transforming growth factor family. It can induce differentiation and proliferation of undifferentiated mesenchymal stem cells into osteoblasts. It also promotes the differentiation and maturation of osteoblasts, and participates in the growth, development and reconstruction of bone and cartilage [43]. On days 7 and 14, the mRNA level of BMP-2 in sTi/VEGF was 2.02 ± 0.18-fold and 3.67 ± 0.13-fold higher compared with that of eTi, and 1.03 ± 0.04-fold and 1.25 ± 0.18-fold higher that in sTi, respectively (Fig. 3D). OCN is expressed at the late stage of osteoblast differentiation and can combine with Ca^{2+} to regulate Ca^{2+} homeostasis and bone mineralization. OCN gene is an important marker of late osteogenesis [44]. On day 7, there was no significant difference in mRNA level of OCN between groups (P > 0.05). On day 14, the mRNA level of OCN was higher by 2.54 ± 0.10-fold in the sTi/VEGF compared with eTi (Fig. 3E). These results show that FMC can affect the osteogenic differentiation of BMSCs at the entire period of osteogenesis.

3.6. Animal experiments

3.6.1. Micro CT

To investigate the bone regeneration potential of sTi/VEGF *in vivo*, we implanted eTi, sTi, and sTi/VEGF into the distal femoral bone defect of rabbits (Fig. S12). The Micro CT analysis was used to observe the formation of new bone in the scaffolds. 3D-reconstructed Micro CT images showed that the amount of new bone in the sTi/VEGF was greater than that in the other groups at 12 week. And it was also observed between the eTi and sTi groups (Fig. 4A). BV/TV represents the area size of bone tissue per unit volume, Tb. Th represents the average thickness of bone trabeculae, Tb. N represents the number of bone trabeculae, and Tb. SP represents the degree of trabecular separation. BV/TV, Tb Th and Tb. N increase indicates an increase in bone mass, while an increase in Tb. SP indicates a decrease in bone mass. The sTi/VEGF groups had significantly higher BV/TV, Tb. Th and Tb. N than the sTi and eTi groups (Figs. 4C, F and 5D), and Tb. SP was significantly lower (Fig. 4E) (P > 0.05). These results, consistent with the results of *in vitro* experiments, demonstrate that titanium alloy scaffolds combined with FMC can promote bone regeneration.

3.6.2. Push-out mechanical test

To measure the bonding strength between different scaffolds and bone tissue, we designed a push-out experiment. As shown in Fig. S13,

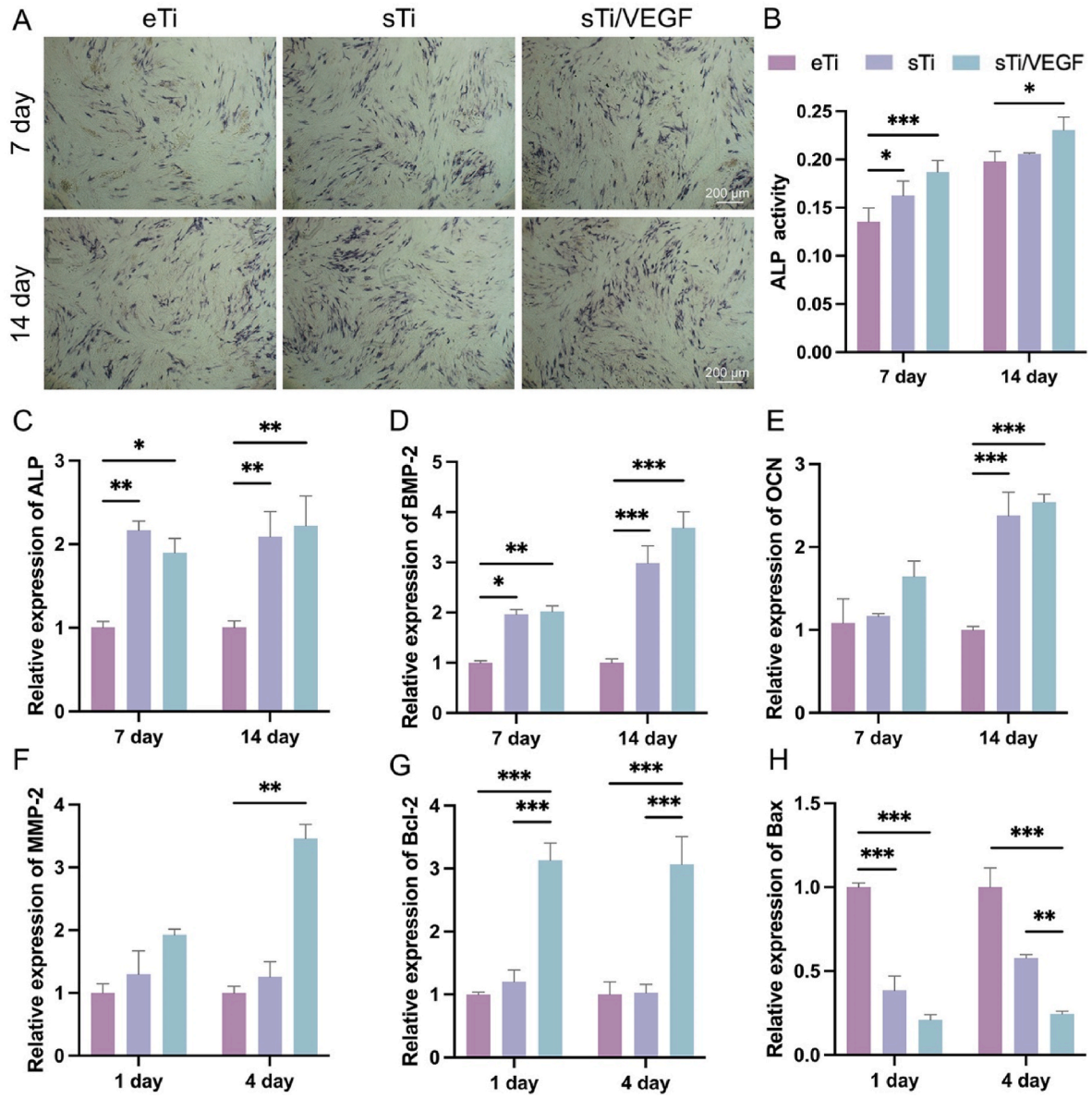

Fig. 3. ALP staining assay and RT-PCR. (A) ALP staining in BMSCs cultured with eTi, sTi, sTi/VEGF for 7 and 14 days. (B) Quantification of the ALP activity (n = 3, *indicates significant differences between the groups, *p < 0.05; **p < 0.01; ***p < 0.001). RT-qPCR analysis of (C) ALP (D) BMP-2 and (E) OCN genes expression in BMSCs cultured with eTi, sTi and sTi/VEGF for 7 and 14 days. RT-qPCR analysis of (F) MMP-2 (G) Bcl-2 and (H) Bax genes expression in HUVECs cultured with eTi, sTi and sTi/VEGF for 1 and 4 days (n = 3, *indicates significant differences between the groups, *p < 0.05; **p < 0.01; ***p < 0.001).

we randomly selected three parallel samples from each group to undergo the push-out test. Subsequently, we performed statistical analysis on the maximum push-out force. The specific experimental data can be found in Table S1, which summarizes the results obtained from the experiment. The result shows that sTi/VEGF group had the strongest binding force with bone tissue, which was 2.36 ± 0.54-fold higher than that of eTi and 1.40 ± 0.12-fold higher than that of sTi (Fig. 4B). The reason for this result is positively correlated with the amount of bone tissue in the scaffold pores. These findings confirm that sTi/VEGF enhances the adhesion and stability of the bone-implant interface by stimulating bone regeneration on the scaffold surface.

3.6.3. Histological analysis

In order to evaluate the growth of new bone on different scaffold surfaces and pores, we obtain histological analysis by VG and Masson staining on specimen sections. For VG staining, as shown in Fig. 5A, only a small amount of new bone tissue was observed on the surface of eTi and sTi, and no significant new bone formation was observed inside the scaffold. In contrast, we observed significant new bone formation on both the surface and interior of sTi/VEGF. In addition, Masson staining was performed to explore the maturity of newly formed bone. At 12 weeks after implantation, new bone (blue) in the defect area grew from the metal micropores of sTi/VEGF, indicating activation of collagen synthesis around the scaffold. Compared with eTi and sTi, significantly more new bone tissue was formed around metal micropores in the sTi/VEGF group. The percentage of new bone tissue in the interface pore area is an important indicator of bone regeneration. The proportion of the area of new bone to interface pores on sections was calculated using Image J software (Fig. 5B and C). Bone ingrowth is the gold standard marker for evaluating bone integration at the microporous interface. The new bone trabeculae grow deep into the pores, interact and fuse with the scaffold through the interconnected pores. Compared with other groups, sTi/VEGF showed excellent bone ingrowth depth and which reached the micropores in the scaffold (Fig. 5D and E). This

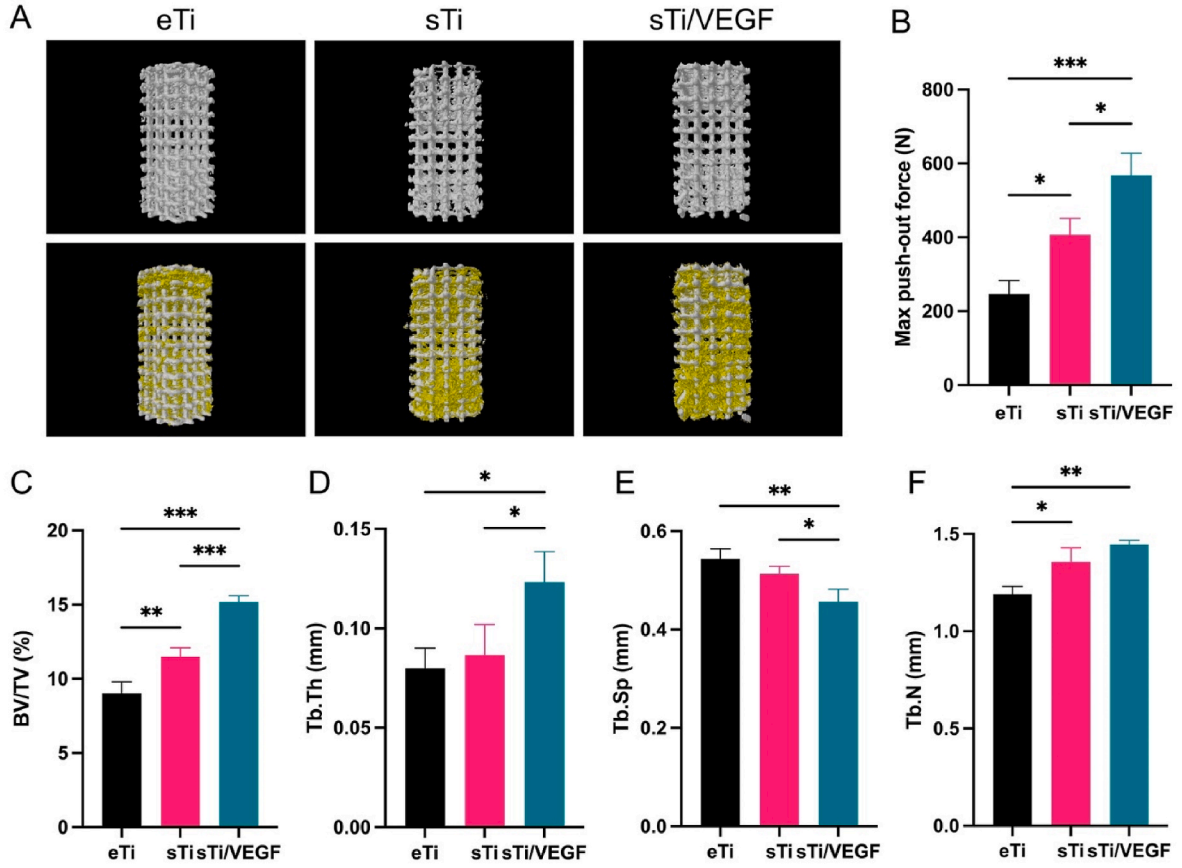

Fig. 4. Micro CT analysis of the defect site. (A) Representative 3D reconstruction images of eTi, sTi and sTi/VEGF 12 weeks post-surgery (yellow represents bone tissue and white represents interfaces in the 3D Micro CT images). (B) Maximum load during the detaching test for eTi, sTi and sTi/VEGF after implantation for 12 weeks. (C–F) Micro CT image analysis of (C) BV/TV, (D) Tb. Th, (E) Tb. Sp, and (F) Tb. N in each group. (n = 3, *indicates significant differences between the groups, *p < 0.05; **p < 0.01; ***p < 0.01). (For interpretation of the references to color in this figure legend, the reader is referred to the Web version of this article.)

further confirmed that sTi/VEGF promote the bone regeneration on the scaffold surface.

3.6.4. *Immunohistochemistry*

Immunohistochemical staining test was conducted to further investigate vascular regeneration and bone regeneration at the scaffold-bone interface. Blood vessels in the tissue were labeled with anti-CD31 and anti-CD34 antibodies, which exhibited a brownish yellow color with round or oval shape. Compared with eTi and sTi group, sTi/VEGF group had higher vascular density (Fig. 6A). In addition, the most important markers of osteogenesis, OCN and Col-1 were also examined. Significant new bone formation was observed around sTi/VEGF (Fig. 6B). The percentage of positive of section was calculated using Image J software (Fig. 6C and D). In general, these results suggested that sTi/VEGF can promote not only the formation of blood vessels but also the regeneration of bone around the scaffold.

4. Discussion

In clinical practice, poor osseointegration is a serious problem faced by joint surgeons [45]. In fact, poor osseointegration causes instability of the prosthesis and reduces its operation life. An important cause of poor osseointegration is lacking of sufficient biological activity on the surface of the prosthesis to induce the proliferation and differentiation of osteoblasts, which prevents the formation of a sufficient amount of bone tissue on the surface of the prosthesis, thereby reducing the binding force between the bone and the prosthesis interface [46]. In addition, the blood supply around the prosthesis is crucial for bone regeneration on the prosthesis surface. Numerous studies and clinical cases have shown that the condition of blood vessels around fractures is a key factor in determining whether fractures heal normally [47]. Combined with the above problems, our team developed a functional mineralized collagen hydrogel that can continuously release VEGF, and combined it with 3D printed titanium alloy scaffold to form a new system. The experimental results demonstrate that this new composite system can promote the regeneration of bone and blood vessels on the scaffold interface through the osteogenic induction of mineralized collagen and the vascular induction of VEGF, thereby achieving the goal of promoting stable binding between bone and implant.

According to previous studies, the osteogenesis behavior of the scaffold is influenced by several factors *in vivo*, including materials used, shape, pore structure and coating [48–51]. We manufactured a porous titanium alloy scaffold with 70% porosity and 765 μm pore diameter by EBM. Compared with the scaffold made by traditional technology, the scaffold made using EBM has a micron-level rough surface, which is more conducive to cell adhesion [52]. Furthermore, the porous structure of the scaffold significantly reduces its elastic modulus and prevents stress shielding [53]. The pore structure inside the scaffold was designed in advance. This is because the porosity in human bone trabecula is 70–90%, and the larger apertures are conducive to the inward growth of bone and blood vessels, which facilitates nutrient exchange [18]. However, the porosity of the scaffold is negatively correlated with its mechanical strength, and excessive porosity is not conducive to early mechanical support during implantation [18]. Based on previous research, we believe that titanium alloy scaffolds with a porosity of 70% can not only ensure inward growth of bone tissue, but also provide sufficient mechanical property [54,55]. We will verify the combination of titanium alloy scaffolds with different pore sizes and porosity with

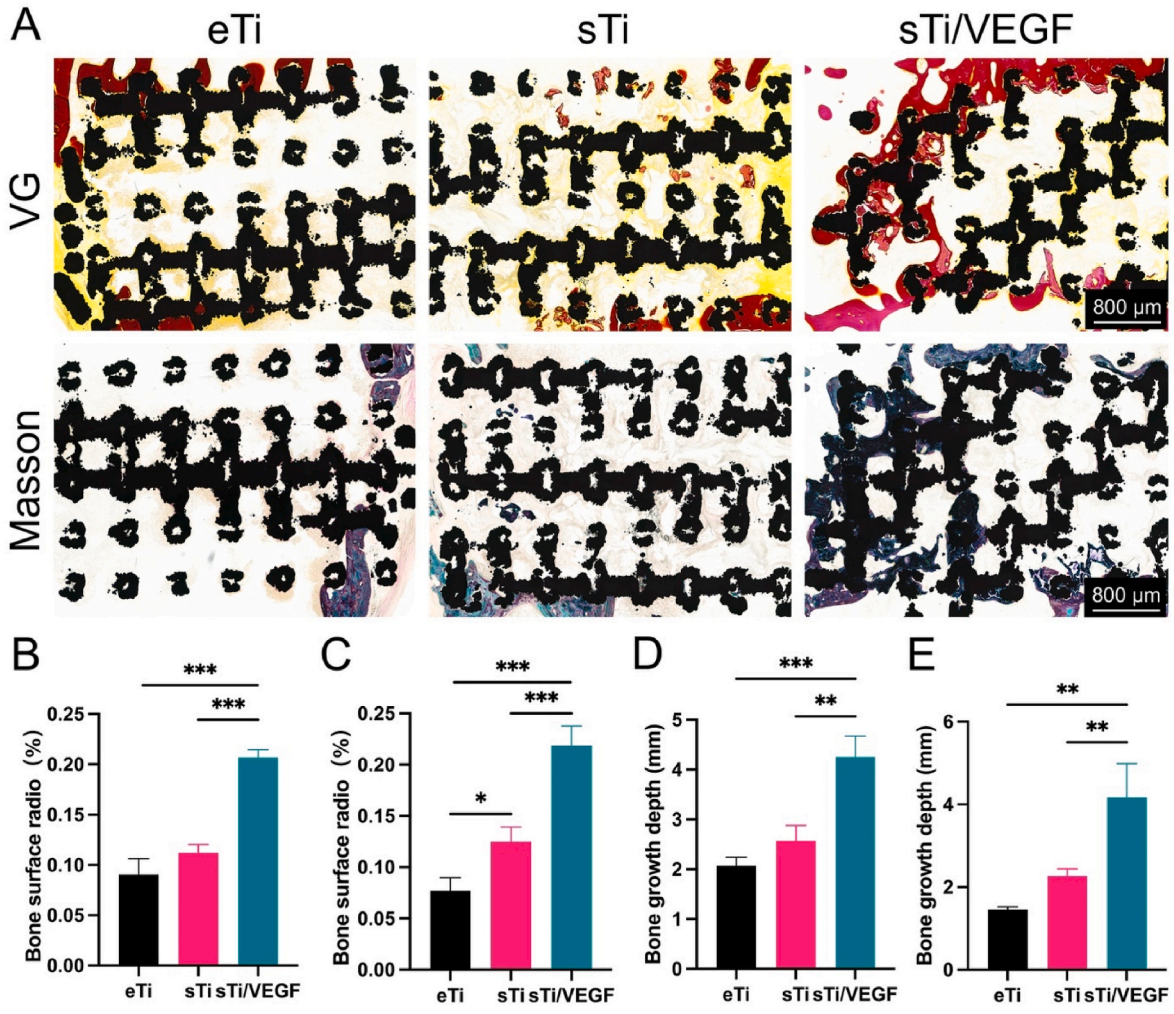

Fig. 5. Histological analysis of local bone regeneration. (A) VG and Masson staining of distal femur defects 12 weeks after eTi, sTi and sTi/VEGF implantation (black indicates Ti_6Al_4V scaffold, red and blue indicates new bone). (B) and (C) The proportion of the area of new bone to pores of interfaces (B: VG, C: Masson). (D) and (E) The depth of the new bone trabecula into the pore (D: VG, E: Masson) (n = 3, *indicates significant differences between the groups, *p < 0.05; **p < 0.01; ***p < 0.01). (For interpretation of the references to color in this figure legend, the reader is referred to the Web version of this article.)

FMC in the future research and identify the most suitable values.

In the past decades, research on collagen materials have received widespread attention. Some researchers believe that a perfect bone tissue substitute material is a biomimetic material with the same composition and structure as autologous bone, and can be safely degraded in the body [56]. At present, researchers have synthesized the basic structure of natural bone tissue - mineralized collagen fibers - through various pathways. Research has shown that MC has almost the same effect as autologous bone in repairing small bone defects [57,58]. This proves that MC has natural bone conduction and bone induction ability. However, research has shown that the mechanical properties of MC materials are extremely poor and cannot provide sufficient mechanical support as a substitute for bone tissue [59]. Furthermore, unmodified mineralized collagen (MC) materials possess a singular function and relatively limited osteogenic ability [56]. Indeed, VEGF (vascular endothelial growth factor) is a growth factor known for its ability to stimulate endothelial cell migration, proliferation, and capillary formation. When VEGF is loaded onto mineralized collagen (MC) materials, it can effectively promote vascular regeneration in the vicinity of the implant. This enhanced vascularization provides an adequate supply of nutrients, oxygen, and other essential factors necessary for the growth and development of new bone tissue. By facilitating vascularization, VEGF-loaded MC materials play a crucial role in promoting the overall osseointegration process [60]. However, it is important to note that using unmodified mineralized collagen (MC) as a carrier for growth factors carries the risk of rapid and uncontrolled release of these factors. This can lead to undesirable effects such as excessive angiogenesis or an inflammatory response. To mitigate this risk, it is crucial to employ appropriate strategies for controlled release of growth factors from the MC carrier, ensuring a sustained and controlled delivery over the desired timeframe. This allows for optimal and targeted effects on vascular regeneration and subsequent bone tissue growth [61].

Research has demonstrated that using substances such as SA can effectively prolong the release time of VEGF in the body while preserving its biological activity. SA-based systems provide a controlled release mechanism that allows for sustained and gradual release of VEGF over an extended period. This controlled release approach helps maintain the biological activity of VEGF and ensures its availability for an extended duration, promoting the desired effects on vascular regeneration and subsequent bone tissue development. By utilizing SA as a carrier, the risk of explosive release of growth factors is minimized, allowing for a more controlled and sustained release profile [62].

Therefore, the utilization of VEGF-loaded sodium alginate (SA)/mineralized collagen (MC) hydrogel represents a novel approach for the functionalization of biomimetic materials. This hydrogel system combines the osteogenic and angiogenic factors, harnessing the synergistic potential of MC and VEGF. MC possesses the ability to promote bone formation, while VEGF is known to stimulate blood vessel growth.

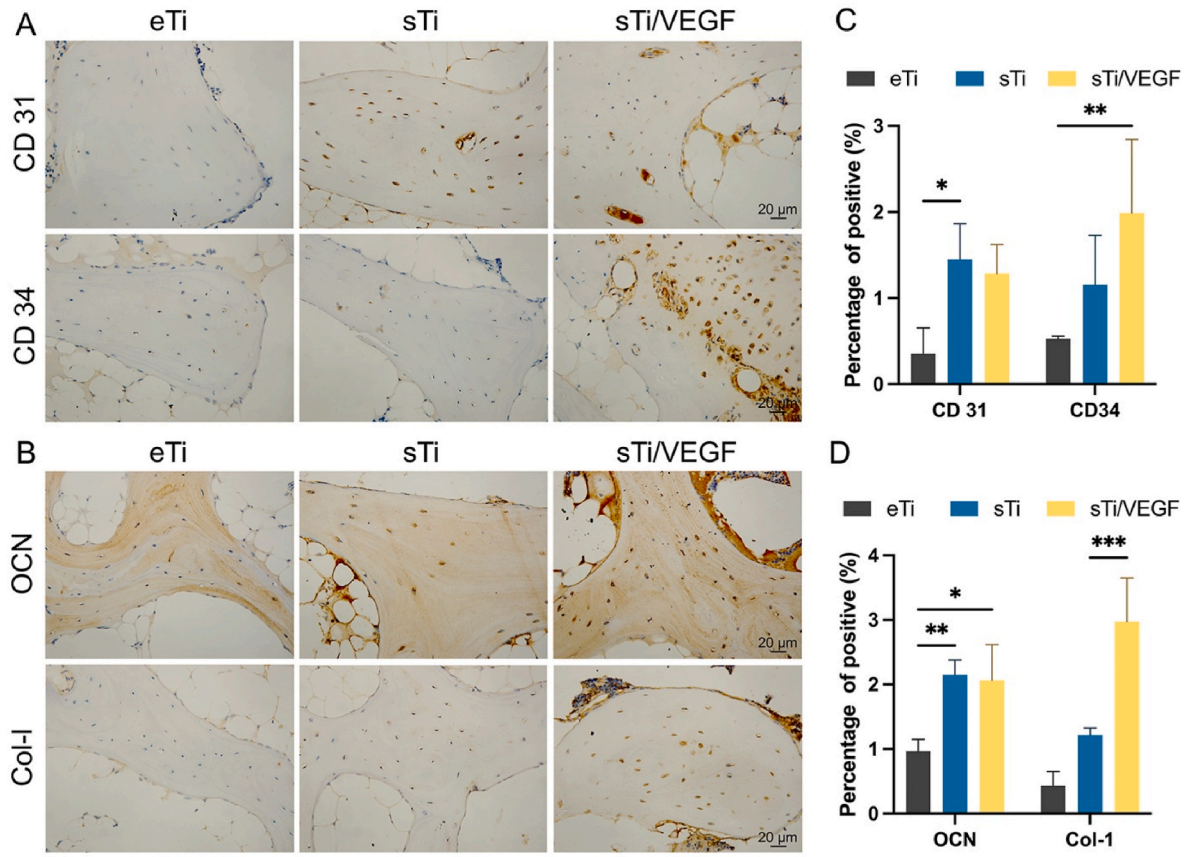

Fig. 6. Immunohistochemical staining for (A) CD 31 and CD34, (B) OCN and Col-1 expression in bone tissues surrounding the eTi, sTi and sTi/VEGF after implantation for 12 weeks (C) Positive percentage of CD31 and CD34 (D) Positive percentage of OCN and Col-1 (n = 3, *indicates significant differences between the groups, *p < 0.05; **p < 0.01; ***p < 0.001).

Moreover, research has shown that MC can upregulate the autophagy process in mesenchymal stem cells (MSCs) mitochondria, thereby promoting osteogenic differentiation. This further highlights the multifaceted benefits of MC in enhancing bone regeneration processes. By incorporating VEGF into the SA/MC hydrogel, we create a biomimetic material that not only supports osteogenesis but also facilitates angiogenesis. This innovative strategy holds promise for promoting the formation of both bone and blood vessels, leading to improved tissue integration and overall functionalization of biomaterials [63].

Another study has demonstrated that mineralized collagen scaffolds can induce time-dependent transcription of bone morphogenetic proteins (BMPs), thereby activating self-BMP signaling through the phosphorylation of Smad 1/5. This process plays a crucial role in promoting osteogenic differentiation and bone formation. The mineralized collagen scaffold provides a favorable microenvironment for the release and activation of BMPs, which are key regulators of bone development and regeneration. The time-dependent transcription of BMPs within the scaffold leads to the activation of Smad 1/5 signaling pathways, ultimately promoting the differentiation of mesenchymal stem cells towards an osteogenic lineage. This finding further underscores the significance of mineralized collagen in promoting bone regeneration and highlights its potential as a biomaterial for tissue engineering applications [64].

In addition, VEGF also plays a crucial role in the process of bone growth and maturation. Research conducted by Murakami et al. has demonstrated that VEGF activates the ERK/RUNX2 signaling pathway, leading to a significant increase in the expression of RUNX2. RUNX2 is a transcription factor that plays a fundamental role in osteoblast differentiation and bone formation. Activation of the ERK/RUNX2 pathway by VEGF promotes osteoblast differentiation and enhances the expression of genes involved in bone matrix synthesis and mineralization. These findings highlight the multifaceted effects of VEGF in bone biology, as it not only promotes angiogenesis but also directly influences osteogenic processes through the activation of signaling pathways such as ERK/RUNX2 [65].

Interestingly, it is intriguing to observe the synergistic effect between the osteogenic mechanism of mineralized collagen (MC) and VEGF. When VEGF activates the Akt/β-catenin signaling pathway, it leads to an increase in bone morphogenetic protein (BMP) levels in mesenchymal stem cells (MSCs). This increase in BMP, mediated by osteoblasts, stimulates osteoblast differentiation through an autocrine system. Furthermore, it also stimulates VEGF production through a positive feedback loop [60]. The functional mineralized collagen (FMC) material effectively integrates the advantages of MC, sodium alginate (SA), and VEGF. This integration allows FMC to exhibit robust osteogenic and angiogenic effects both *in vivo* and *in vitro*. The combination of MC's osteogenic properties, SA's controlled release capabilities, and VEGF's angiogenic potential contributes to the comprehensive and synergistic effects observed with FMC. These findings highlight the potential of FMC as a biomaterial that can promote both bone regeneration and vascularization, making it a promising candidate for various tissue engineering applications.

We observed through SEM that FMC was completely filled into the pores of the scaffold and formed a uniform and rough surface. EDS, XRD, and FTIR results confirmed the presence of FMC on the scaffold surface. ELISA was used to detect the release behavior of VEGF. We found that VEGF from the FMC was fast in the first week, with a slow release rate in the subsequent time, reaching about 80% at the end of 28 days. A similar degradation behavior of hydrogel was observed in rats. Therefore, we speculate that the release of VEGF is linked to the degradation of FMC. The larger volume of the hydrogel at the beginning could lead to a larger

contact area with the surrounding environment, resulting in faster degradation speed. However, with time, the volume of hydrogel becomes smaller, slowing down the degradation rate.

Cell viability experiments confirmed the excellent biocompatibility of sTi/VEGF. Notably, the results of live staining and CCK-8 showed that compared with the scaffold without FMC, there was a higher number of living cells in the microporous structure of sTi and sTi/VEGF, and their proliferation rate was faster. It shows that the components of sTi/VEGF have no obvious cytotoxicity and promote cell growth and proliferation. This is because FMC can provide more space for cell reproduction than smooth titanium alloy surfaces. In addition, the behavior of HUVECs indicates that sTi/VEGF can promote vascular remodeling by inducing targeted migration of vascular endothelial cells. In general, the migration rate of endothelial cells determined the speed of vascular reconstruction around the bone-implant interface, higher vascularization which provided favorable conditions for bone tissue regeneration. In addition, we assessed the effect of sTi/VEGF on osteogenic differentiation of BMSCs cells using ALP staining, quantitative analysis and PCR experiments. sTi/VEGF improved the ALP content and significantly increased osteogenesis-related genes expression of BMSCs in sTi and sTi/VEGF groups compared with the eTi group.

In animal experiments, cylindrical bone defects were made on the external femoral epicondyle of our rabbits for implantation of scaffolds. After 12 weeks, the femoral specimen with scaffold was harvest and observed using micro CT to assess the growth of bone tissue in the micropores and surface of the scaffold. Compared with eTi and sTi, there was a large amount of bone tissue in and around the sTi/VEGF scaffold. The mechanical push out experiment verified that sTi/VEGF had the strongest binding force with the surrounding bone tissue. To further observe the inward growth of bone, we sectioned the titanium alloy scaffold and stained it with VG and Masson. The results showed that compared with eTi the amount of new bone tissue in the sTi/VEGF was larger. Finally, immunohistochemical staining showed that sTi/VEGF successfully induced the expression of osteogenic and angiogenic marker proteins. Taken together, these results prove that sTi/VEGF can induce bone and vascular regeneration and promote bone integration at the metal microporous interface *in vivo*.

In follow-up research, we will assess the bone integration of this bionic interface under pathological conditions and further improve it. For example, strontium ion or bisphosphonate can be added to the FMC to promote osseointegration under osteoporosis. In addition, we will further optimize the release rate of biological factors or agents loaded in the hydrogel to ensure the biological safety of implants. Our ultimate goal is to develop a new generation of intelligent hydrogel/metal microporous system that can adapt to different people.

5. Conclusion

In this study, we designed a functionalized mineralized collagen hydrogel and filled it into the pores of 3D printed porous titanium alloy scaffold. Compared with a single mineralized collagen material, the addition of sodium alginate and VEGF improved the mechanical properties and angiogenesis ability of mineralized collagen. This new mineralized collagen material enhances the osteogenic differentiation of BMSCs and the directional migration of HUVECs. When a titanium alloy scaffold filled with this material is implanted into a bone defect, it can promote bone and vascular regeneration through the continuous release of VEGF and the osteogenic induction of mineralized collagen, ultimately achieving the goal of promoting bone osseointegration. Our results provide a new strategy for the development and application of new mineralized collagen materials.

CRediT authorship contribution statement

Xiao Sheng: Conceptualization, Investigation, Writing - original draft, preparation. **He Liu:** Data curation, Writing - review & editing. **Yu Xu:** Data curation, Validation. **Zhonghan Wang:** Validation, Methodology. **Weimin Zhang:** Visualization, Software. **Chen Li:** Supervision, Funding acquisition, Conceptualization, Writing - review & editing. **Jincheng Wang:** Conceptualization, Validation, Methodology.

Declaration of competing interest

The authors declare that they have no known competing financial interests or personal relationships that could have appeared to influence the work reported in this paper.

Data availability

Data will be made available on request.

Acknowledgements

This work was supported by the Science and Technology Research Project of Education Department of Jilin Province (Grant No. JJKH20211172KJ), the National Natural Science Foundation of China (Grant Nos. 82001971, 82372391, U21A2099, U23A20523), Project of "Medical+X" interdisciplinary innovation team of Norman Bethune Health Science Center of Jilin Universtiy (Grant No. 2022JBGS06). Scientific Development Program of Jilin Province (Grant Nos. YDZJ202301ZYTS031), The Science and Technology Development Program of Jilin Province (Grant No. 20210101319JC), Bethune Plan of Jilin University (Grant No. 2023B10). Project of youth interdisciplinary innovation team of Jilin University (Grant No. 419070623054).

Appendix A. Supplementary data

Supplementary data to this article can be found online at https://doi.org/10.1016/j.mtbio.2023.100896.

References

[1] N. Liu, C.M. Zheng, Q.L. Wang, Z.P. Huang, Treatment of non-traumatic avascular necrosis of the femoral head, Exp. Ther. Med. 23 (2022), https://doi.org/10.3892/etm.2022.11250 (Review).
[2] M. Betsch, M. Tingart, A. Driessen, V. Quack, B. Rath, Total hip replacement in avascular femoral head necrosis, Orthopä 47 (2018) 751–756, https://doi.org/10.1007/s00132-018-3617-5.
[3] S. Kurtz, K. Ong, E. Lau, F. Mowat, M. Halpern, Projections of primary and revision hip and knee arthroplasty in the United States from 2005 to 2030, J. Bone Jt. Surg.-Am. 89A (2007) 780–785, https://doi.org/10.2106/jbjs.F.00222.
[4] M. Sloan, A. Premkumar, N.P. Sheth, Projected volume of primary total joint arthroplasty in the US, 2014 to 2030, J. Bone Jt. Surg.-Am. 100 (2018) 1455–1460, https://doi.org/10.2106/jbjs.17.01617.
[5] S. Kurtz, F. Mowat, K. Ong, N. Chan, E. Lau, M. Halpern, Prevalence of primary and revision total hip and knee arthroplasty in the United States from 1990 through 2002, J. Bone Jt. Surg.-Am. 87A (2005) 1487–1497, https://doi.org/10.2106/jbjs.D.02441.
[6] Y. Gao, Q. Ma, Bacterial infection microenvironment-responsive porous microspheres by microfluidics for promoting anti-infective therapy, Smart Med. 1 (2022), https://doi.org/10.1002/smmd.20220012.
[7] R. Zhou, Y. Han, J.Y. Cao, M. Li, G.R. Jin, Y.Z. Du, H.T. Luo, Y.C. Yang, L.Z. Zhang, B. Su, Enhanced osseointegration of hierarchically structured Ti implant with electrically bioactive SnO2-TiO2 bilayered surface, ACS Appl. Mater. Interfaces 10 (2018) 30191–30200, https://doi.org/10.1021/acsami.8b10928.
[8] R. Smeets, B. Stadlinger, F. Schwarz, B. Beck-Broichsitter, O. Jung, C. Precht, F. Kloss, A. Grobe, M. Heiland, T. Ebker, Impact of dental implant surface modifications on osseointegration, BioMed Res. Int. (2016) 2016, https://doi.org/10.1155/2016/6285620.
[9] Y. Kfoury, D.T. Scadden, Mesenchymal cell contributions to the stem cell niche, Cell Stem Cell 16 (2015) 239–253, https://doi.org/10.1016/j.stem.2015.02.019.
[10] A.F. Mavrogenis, R. Dimitriou, J. Parvizi, G.C. Babis, Biology of implant osseointegration, J. Musculoskelet. Neuronal Interact. 9 (2009) 61–71.
[11] A. Insua, A. Monje, H.L. Wang, R.J. Miron, Basis of bone metabolism around dental implants during osseointegration and peri-implant bone loss, J. Biomed. Mater. Res. 105 (2017) 2075–2089, https://doi.org/10.1002/jbm.a.36060.
[12] Y. Zhu, B. Kong, R. Liu, Y. Zhao, Developing biomedical engineering technologies for reproductive medicine, Smart Med. 1 (2022), https://doi.org/10.1002/smmd.20220006.

[13] D. Zhang, W. Li, Y. Shang, L. Shang, Programmable microfluidic manipulations for biomedical applications, Eng. Regenerat. 3 (2022) 258–261, https://doi.org/10.1016/j.engreg.2022.06.001.

[14] S.V. Murphy, A. Atala, 3D bioprinting of tissues and organs, Nat. Biotechnol. 32 (2014) 773–785, https://doi.org/10.1038/nbt.2958.

[15] M.C. Ratri, A.I. Brilian, A. Setiawati, H.T. Nguyen, V. Soum, K. Shin, Recent advances in regenerative tissue fabrication: tools, materials, and microenvironment in hierarchical aspects, Adv. Nanobiomed Res. 1 (2021), https://doi.org/10.1002/anbr.202000088.

[16] C. Hu, D. Ashok, D.R. Nisbet, V. Gautam, Bioinspired surface modification of orthopedic implants for bone tissue engineering, Biomaterials 219 (2019), 119366, https://doi.org/10.1016/j.biomaterials.2019.119366.

[17] X. Sheng, A. Wang, Z. Wang, H. Liu, J. Wang, C. Li, Advanced surface modification for 3D-printed titanium alloy implant interface functionalization, Front. Bioeng. Biotechnol. 10 (2022), 850110, https://doi.org/10.3389/fbioe.2022.850110.

[18] Z. Wang, C. Wang, C. Li, Y. Qin, L. Zhong, B. Chen, Z. Li, H. Liu, F. Chang, J. Wang, Analysis of factors influencing bone ingrowth into three-dimensional printed porous metal scaffolds: a review, J. Alloys Compd. 717 (2017) 271–285, https://doi.org/10.1016/j.jallcom.2017.05.079.

[19] S. Arabnejad, B. Johnston, M. Tanzer, D. Pasini, Fully porous 3D printed titanium femoral stem to reduce stress-shielding following total hip arthroplasty, J. Orthop. Res. 35 (2017) 1774–1783, https://doi.org/10.1002/jor.23445.

[20] S. Gomez, M.D. Vlad, J. Lopez, E. Fernandez, Design and properties of 3D scaffolds for bone tissue engineering, Acta Biomater. 42 (2016) 341–350, https://doi.org/10.1016/j.actbio.2016.06.032.

[21] Z.H. Wang, C.Y. Wang, C. Li, Y.G. Qin, L. Zhong, B.P. Chen, Z.Y. Li, H. Liu, F. Chang, J.C. Wang, Analysis of factors influencing bone ingrowth into three-dimensional printed porous metal scaffolds: a review, J. Alloys Compd. 717 (2017) 271–285, https://doi.org/10.1016/j.jallcom.2017.05.079.

[22] Z.Y. Qiu, Y. Cui, C.S. Tao, Z.Q. Zhang, P.F. Tang, K.Y. Mao, X.M. Wang, F.Z. Cui, Mineralized collagen: rationale, current status, and clinical applications, Materials 8 (2015) 4733–4750, https://doi.org/10.3390/ma8084733.

[23] F. Nudelman, K. Pieterse, A. George, P.H.H. Bomans, H. Friedrich, L.J. Brylka, P.A. J. Hilbers, G. de With, N.A.J.M. Sommerdijk, The role of collagen in bone apatite formation in the presence of hydroxyapatite nucleation inhibitors, Nat. Mater. 9 (2010) 1004–1009, https://doi.org/10.1038/nmat2875.

[24] H.P. Schwarcz, D.M. Binkley, L. Luo, K. Grandfield, A search for apatite crystals in the gap zone of collagen fibrils in bone using dark-field illumination, Bone 135 (2020), 115304, https://doi.org/10.1016/j.bone.2020.115304.

[25] Y. Liu, D. Luo, T. Wang, Hierarchical structures of bone and bioinspired bone tissue engineering, Small 12 (2016) 4611–4632, https://doi.org/10.1002/smll.201600626.

[26] J.H. Bradt, M. Mertig, A. Teresiak, W. Pompe, Biomimetic mineralization of collagen by combined fibril assembly and calcium phosphate formation, Chem. Mater. 11 (1999) 2694–2701, https://doi.org/10.1021/cm991002p.

[27] L.M. Ma, X.L. Wang, N.R. Zhao, Y. Zhu, Z.Y. Qiu, Q.T. Li, Y. Zhou, Z.F. Lin, X. Li, X. L. Zeng, H. Xia, S.Z. Zhong, Y. Zhang, Y.J. Wang, C.B. Mao, Integrating 3D printing and biomimetic mineralization for personalized enhanced osteogenesis, angiogenesis, and osteointegration, ACS Appl. Mater. Interfaces 10 (2018) 42146–42154, https://doi.org/10.1021/acsami.8b17495.

[28] L. Zhong, Y. Qu, K. Shi, B.Y. Chu, M.Y. Lei, K.K. Huang, Y.C. Gu, Z.Y. Qian, Biomineralized polymer matrix composites for bone tissue repair: a review, Sci. China Chem. 61 (2018) 1553–1567, https://doi.org/10.1007/s11426-018-9324-0.

[29] J. Venkatesan, I. Bhatnagar, P. Manivasagan, K.H. Kang, S.K. Kim, Alginate composites for bone tissue engineering: a review, Int. J. Biol. Macromol. 72 (2015) 269–281, https://doi.org/10.1016/j.ijbiomac.2014.07.008.

[30] X. Sheng, C. Li, Z. Wang, Y. Xu, Y. Sun, W. Zhang, H. Liu, J. Wang, Advanced applications of strontium-containing biomaterials in bone tissue engineering, Mater. Today Bio 20 (2023), https://doi.org/10.1016/j.mtbio.2023.100636.

[31] W. Su, L. Ma, Y. Ran, X. Ma, Z. Yi, G. Chen, X. Chen, X. Li, Alginate-assisted mineralization of collagen by collagen reconstitution and calcium phosphate formation, ACS Biomater. Sci. Eng. 6 (2020) 3275–3286, https://doi.org/10.1021/acsbiomaterials.9b01841.

[32] T.K. Giri, D. Thakur, A. Alexander, Ajazuddin, H. Badwaik, D.K. Tripathi, Alginate based hydrogel as a potential biopolymeric carrier for drug delivery and cell delivery systems: present status and applications, Curr. Drug Deliv. 9 (2012) 539–555.

[33] M. Quade, S. Knaack, A.R. Akkineni, A. Gabrielyan, A. Lode, A. Rosen-Wolff, M. Gelinsky, Central growth factor loaded depots in bone tissue engineering scaffolds for enhanced cell attraction, Tissue Eng. 23 (2017) 762–772, https://doi.org/10.1089/ten.tea.2016.0483.

[34] Z. Che, Y. Sun, W. Luo, L. Zhu, Y. Li, C. Zhu, T. Liu, L. Huang, Bifunctionalized hydrogels promote angiogenesis and osseointegration at the interface of three-dimensionally printed porous titanium scaffolds, Mater. Des. 223 (2022), https://doi.org/10.1016/j.matdes.2022.111118.

[35] M. Quade, P. Munch, A. Lode, S. Duin, C. Vater, A. Gabrielyan, A. Rosen-Wolff, M. Gelinsky, The secretome of hypoxia conditioned hMSC loaded in a central depot induces chemotaxis and angiogenesis in a biomimetic mineralized collagen bone replacement material, Adv. Healthcare Mater. 9 (2020), https://doi.org/10.1002/adhm.201901426.

[36] Y. Bai, Y. Leng, G. Yin, X. Pu, Z. Huang, X. Liao, X. Chen, Y. Yao, Effects of combinations of BMP-2 with FGF-2 and/or VEGF on HUVECs angiogenesis *in vitro* and CAM angiogenesis *in vivo*, Cell Tissue Res. 356 (2014) 109–121, https://doi.org/10.1007/s00441-013-1781-9.

[37] B.H. Grue, S.P. Veres, Use of tendon to produce decellularized sheets of mineralized collagen fibrils for bone tissue repair and regeneration, J. Biomed. Mater. Res. B Appl. Biomater. 108 (2020) 845–856, https://doi.org/10.1002/jbm.b.34438.

[38] B. Iqbal, Z. Sarfaraz, N. Muhammad, P. Ahmad, J. Iqbal, Z.U.H. Khan, G. Gonfa, F. Iqbal, A. Jamal, A. Rahim, Ionic liquid as a potential solvent for preparation of collagen-alginate-hydroxyapatite beads as bone filler, J. Biomater. Sci. Polym. Ed. 29 (2018) 1168–1184, https://doi.org/10.1080/09205063.2018.1443604.

[39] T.L. Haas, Endothelial cell regulation of matrix metalloproteinases, Can. J. Physiol. Pharmacol. 83 (2005) 1–7, https://doi.org/10.1139/y04-120.

[40] Z. Kohandel, T. Farkhondeh, M. Aschner, S. Samarghandian, Molecular targets for the management of gastrointestinal cancer using melatonin, a natural endogenous body hormone, Biomed. Pharmacother. 140 (2021), https://doi.org/10.1016/j.biopha.2021.111782.

[41] M. Gagliardi, A.T. Ashizawa, Making sense of antisense oligonucleotide therapeutics targeting bcl-2, Pharmaceutics 14 (2022), https://doi.org/10.3390/pharmaceutics14010097.

[42] U. Sharma, D. Pal, R. Prasad, Alkaline phosphatase: an overview, Indian J. Clin. Biochem. : Indian J. Clin. Biochem. 29 (2014) 269–278, https://doi.org/10.1007/s12291-013-0408-y.

[43] E. Balint, D. Lapointe, H. Drissi, C. van der Meijden, D.W. Young, A.J. van Wijnen, J.L. Stein, G.S. Stein, J.B. Lian, Phenotype discovery by gene expression profiling: mapping of biological processes linked to BMP-2-mediated osteoblast differentiation, J. Cell. Biochem. 89 (2003) 401–426, https://doi.org/10.1002/jcb.10515.

[44] T. Komori, Functions of osteocalcin in bone, pancreas, testis, and muscle, Int. J. Mol. Sci. 21 (2020), https://doi.org/10.3390/ijms21207513.

[45] L. Wang, H.Z. He, X. Yang, Y.C. Zhang, S.L. Xiong, C. Wang, X. Yang, B. Chen, Q. Wang, Bimetallic ions regulated PEEK of bone implantation for antibacterial and osteogenic activities, Mater. Today Adv. 12 (2021), https://doi.org/10.1016/j.mtadv.2021.100162.

[46] M.Z. Ibrahim, A. Halilu, A.A.D. Sarhan, T.Y. Kuo, F. Yusuf, M.O. Shaikh, M. Hamdi, In-vitro viability of laser cladded Fe-based metallic glass as a promising bioactive material for improved osseointegration of orthopedic implants, Med. Eng. Phys. 102 (2022), https://doi.org/10.1016/j.medengphy.2022.103782.

[47] M.M. Menger, M.W. Laschke, M. Orth, T. Pohlemann, M.D. Menger, T. Histing, Vascularization strategies in the prevention of nonunion formation, Tissue Eng. B Rev. 27 (2021) 107–132, https://doi.org/10.1089/ten.teb.2020.0111.

[48] J.P. Zheng, L.J. Chen, D.Y. Chen, C.S. Shao, M.F. Yi, B. Zhang, Effects of pore size and porosity of surface-modified porous titanium implants on bone tissue ingrowth, Trans. Nonferrous Metals Soc. China 29 (2019) 2534–2545, https://doi.org/10.1016/s1003-6326(19)65161-7.

[49] M.H. Elahinia, M. Hashemi, M. Tabesh, S.B. Bhaduri, Manufacturing and processing of NiTi implants: a review, Prog. Mater. Sci. 57 (2012) 911–946, https://doi.org/10.1016/j.pmatsci.2011.11.001.

[50] S. Bauer, P. Schmuki, K. von der Mark, J. Park, Engineering biocompatible implant surfaces Part I: materials and surfaces, Prog. Mater. Sci. 58 (2013) 261–326, https://doi.org/10.1016/j.pmatsci.2012.09.001.

[51] S.B. Goodman, Z.Y. Yao, M. Keeney, F. Yang, The future of biologic coatings for orthopaedic implants, Biomaterials 34 (2013) 3174–3183, https://doi.org/10.1016/j.biomaterials.2013.01.074.

[52] D. Mah, M.H. Pelletier, V. Lovric, W.R. Walsh, Corrosion of 3D-printed orthopaedic implant materials, Ann. Biomed. Eng. 47 (2019) 162–173, https://doi.org/10.1007/s10439-018-02111-1.

[53] V.K. Meena, P. Kalra, R.K. Sinha, Finite element study on the influence of pore size and structure on stress shielding effect of additive manufactured spinal cage, Comput. Methods Biomech. Biomed. Eng. 25 (2022) 566–577, https://doi.org/10.1080/10255842.2021.1970142.

[54] Y. Li, Y. Liu, H. Bai, R. Li, J. Shang, Z. Zhu, L. Zhu, C. Zhu, Z. Che, J. Wang, H. Liu, L. Huang, Sustained release of VEGF to promote angiogenesis and osteointegration of three-dimensional printed biomimetic titanium alloy implants, Front. Bioeng. Biotechnol. 9 (2021), 757767, https://doi.org/10.3389/fbioe.2021.757767.

[55] H. Bai, Y. Cui, C. Wang, Z. Wang, W. Luo, Y. Liu, Y. Leng, J. Wang, Z. Li, H. Liu, 3D printed porous biomimetic composition sustained release zoledronate to promote osteointegration of osteoporotic defects, Mater. Des. 189 (2020), https://doi.org/10.1016/j.matdes.2020.108513.

[56] X.J. Zhu, C.Y. Wang, H.T. Bai, J.X. Zhang, Z.H. Wang, Z.H. Li, X. Zhao, J.C. Wang, H. Liu, Functionalization of biomimetic mineralized collagen for bone tissue engineering, Mater. Today Bio 20 (2023), https://doi.org/10.1016/j.mtbio.2023.100660.

[57] K. Lian, H. Lu, X. Guo, F. Cui, Z. Qiu, S. Xu, The mineralized collagen for the reconstruction of intra-articular calcaneal fractures with trabecular defects, Biomatter 3 (2013), https://doi.org/10.4161/biom.27250.

[58] X. Yu, L. Xu, F.Z. Cui, Y. Qu, X.J. Lian, X.M. Wang, Y. Wang, Clinical evaluation of mineralized collagen as a bone graft substitute for anterior cervical intersomatic fusion, J. Biomater. Tissue Eng. 2 (2012) 170–176, https://doi.org/10.1166/jbt.2012.1041.

[59] D. Qin, N. Wang, X.G. You, A.D. Zhang, X.G. Chen, Y. Liu, Collagen-based biocomposites inspired by bone hierarchical structures for advanced bone regeneration: ongoing research and perspectives, Biomater. Sci. 10 (2022) 318–353, https://doi.org/10.1039/d1bm01294k.

[60] K. Liu, C.X. Meng, Z.Y. Lv, Y.J. Zhang, J. Li, K.Y. Li, F.Z. Liu, B. Zhang, F.Z. Cui, Enhancement of BMP-2 and VEGF carried by mineralized collagen for mandibular bone regeneration, Regenerat. Biomater. 7 (2020) 435–440, https://doi.org/10.1093/rb/rbaa022.

[61] S. Knaack, A. Lode, B. Hoyer, A. Roesen-Wolff, A. Gabrielyan, I. Roeder, M. Gelinsky, Heparin modification of a biomimetic bone matrix for controlled

release of VEGF, J. Biomed. Mater. Res. 102 (2014) 3500–3511, https://doi.org/10.1002/jbm.a.35020.

[62] M. Quade, S. Knaack, A.R. Akkineni, A. Gabrielyan, A. Lode, A. Roesen-Wolff, M. Gelinsky, Central growth factor loaded depots in bone tissue engineering scaffolds for enhanced cell attraction, Tissue Eng. 23 (2017) 762–772, https://doi.org/10.1089/ten.tea.2016.0483.

[63] M.C. Wan, X.Y. Tang, J. Li, P. Gao, F. Wang, M.J. Shen, J.T. Gu, F. Tay, J.H. Chen, L.N. Niu, Y.H. Xiao, K. Jiao, Upregulation of mitochondrial dynamics is responsible for osteogenic differentiation of mesenchymal stem cells cultured on self-mineralized collagen membranes, Acta Biomater. 136 (2021) 137–146, https://doi.org/10.1016/j.actbio.2021.09.039.

[64] X.Y. Ren, V. Tu, D. Bischoff, D.W. Weisgerber, M.S. Lewis, D.T. Yamaguchi, T. A. Miller, B.A.C. Harley, J.C. Lee, Nanoparticulate mineralized collagen scaffolds induce *in vivo* bone regeneration independent of progenitor cell loading or exogenous growth factor stimulation, Biomaterials 89 (2016) 67–78, https://doi.org/10.1016/j.biomaterials.2016.02.020.

[65] J. Murakami, M. Ishii, F. Suehiro, K. Ishihata, N. Nakamura, M. Nishimura, Vascular endothelial growth factor-C induces osteogenic differentiation of human mesenchymal stem cells through the ERK and RUNX2 pathway, Biochem. Biophys. Res. Commun. 484 (2017) 710–718, https://doi.org/10.1016/j.bbrc.2017.02.001.